ICARUS **129,** 482–497 (1997)
ARTICLE NO. IS975772

# Spatially Resolved Images of Titan by Means of Adaptive Optics

M. Combes, L. Vapillon, E. Gendron, A. Coustenis, O. Lai, R. Wittemberg, and R. Sirdey

*Département de Recherche Spatiale (DESPA)—Unité Associée au CNRS no. 264, Observatoire de Paris, 92195 Meudon Cedex, France*
E-mail: mcombes@obspm.fr

Received January 30, 1997; revised April 25, 1997

**Images of Titan were acquired with the ADONIS adaptive optics system installed at the ESO 3.6-m telescope in La Silla (Chile). The near-infrared range from 1–2.5 $\mu$m was covered in 1994 and 1995 in the methane atmospheric windows at 1.3, 1.6, and 2.0 $\mu$m with narrow-band filters and CVF. Diffraction-limited images were obtained (0.14 arcsec at 2 $\mu$m), thus allowing us to resolve the Titan disk. We have corrected the images for systematic effects, removed center-to-limb variation, and applied deconvolution processes to our data. The contrast on the images is on the order of 30%. Both the leading and trailing hemispheres were observed. The 2-$\mu$m images presented in this paper show a broad bright feature on the surface of Titan's leading hemisphere (near 114° LCM), which is in agreement with the HST images and with spectroscopy performed at these longitudes from the ground that show a higher geometric albedo on Titan's leading side. High-quality flat fielding of our data has highlighted the presence of at least two main bright spots within the equatorial region. The trailing hemisphere of Titan's surface is not completely dark but shows brightness near the poles, with some north-to-south asymmetry. The northern latitudes are uniformly brighter than the lower equatorial and southern latitudes (factor of about 2). Our results bring new constraints on the models of the satellite's surface.**


## 1. INTRODUCTION

A few months before the launch of the Cassini–Huygens ESA–NASA mission, interest in Titan, its complex atmosphere, and the still-controversial nature of its surface remained at a high level in the scientific community.

The purpose of this paper is to report recent advances in observations of Titan which improve our understanding of the physical structure and the chemical nature of the satellite's surface, thus helping to optimize the Cassini–Huygens observing sequences, as well as to prepare short-term ground-based supporting programs with the forthcoming 8-m class telescopes, in particular the VLT in Chile. Spatially resolved images of Titan have been recorded to date at the 3.6-m ESO telescope, equipped with the COME-ON PLUS system of adaptive optics, in October 1993, September 1994, October 1995, and November 1996. The 1993 and 1994 observations mainly relate to the leading hemisphere of Titan close to the Greatest Eastern Elongation. In this paper, 1994 observations in the 2-$\mu$m range will be reported as well as some preliminary reduced 1995 images (of the trailing hemisphere) which can improve the interpretation of the data and constrain the nature of the surface. The more recent images will be extensively discussed in a forthcoming paper (Combes *et al.* 1997, in preparation).

For a comprehensive review of our current understanding of Titan's surface physics, the reader is referred to Lunine (1993). Nevertheless, note that the interest for investigations of the physical, chemical, and morphological nature of Titan's surface is basically linked to the complex photochemistry which takes place in Titan's atmosphere. This complex photochemistry leads to the production of highly complicated and stable organic molecules which are supposed to have accumulated, over billions of years, on the ground. In the temperature and pressure conditions prevailing on Titan's surface, the methane–ethane and molecular nitrogen mixture should be in liquid state, with poor but existing solving capabilities which may favor even more complex organic, and perhaps prebiotic, chemistry.

Models assuming a surface covered by a global ocean of liquid hydrocarbons and nitrogen have been proposed based on theoretical considerations and on the results of the Voyager 1 flyby (Sagan *et al.* 1982, Lunine *et al.* 1983, Lellouch *et al.* 1989). In contrast, radar observations (Muhleman *et al.* 1990), supported by infrared photometric and spectroscopic data, suggest that the surface should be heterogeneous and mostly solid (ice) (Griffith and Owen 1992, Noll *et al.* 1993, Lemmon *et al.* 1993, 1995, Coustenis *et al.* 1995, 1997).

Obviously, direct imaging of the ground of Titan provides unique opportunities to help resolve this controversial question. But the atmosphere of Titan is opaque at most wavelengths, either due to molecular absorptions (mainly methane bands) or to backscattering of the incoming solar light by stratospheric aerosols as shown in the



0019-1035/97 $25.00

Voyager 1 visible images. In these images, only a faint hemispherical albedo asymmetry could be observed—the northern hemisphere appearing darker than the southern. This asymmetric structure has been connected with a large temperature field asymmetry and interpreted as being due to dynamical inertia forcing the atmosphere to lag behind the insolation (Flasar and Conrath 1990) and/or to the observed asymmetric distribution of the opacity sources (Bézard *et al.* 1995). The Titan North Pole showed enhanced haze and minor gaseous components at the time of the Voyager encounter (Nov. 1980) with respect to the south (Coustenis *et al.* 1991, Coustenis and Bézard 1995). This situation is expected to undergo seasonal effects, so that two Titan seasons (or 15 years) later, in 1995, this asymmetry is predicted to be reversed. The reversal was actually observed first by Caldwell *et al.* (1992). In the visible, the South Pole should at present appear darker, but in the near-infrared the effect is reversed.

During the definition phase of the Cassini–Huygens mission, Combes and Encrenaz (1984) and independently Tomasko *et al.* (1984) have shown that transparent windows should exist in Titan's atmosphere at wavelengths where the absorption by methane and other hydrocarbons is low and where—simultaneously—the extinction due to scattering is faint. Indeed two antagonistic behaviors are competing: the incoming solar flux, and as a consequence the recorded signal, is rapidly decreasing with increasing wavelengths while the attenuation or smoothing of the contrast of surface features due to atmospheric scattering is rapidly increasing with decreasing wavelengths. The most favorable spectral ranges lie in the near infrared around 4.9, 2.0, 1.6, 1.3, 1.1, 0.9, and 0.8 $\mu$m, where atmospheric ''windows'' occur between strong methane absorption bands and where the scattering optical depth remains significantly below unity. This has been confirmed by the various photometric and spectroscopic infrared observations, quoted above, suggesting surface heterogeneities. Observations of Titan's surface will be performed in these windows by the descent imager spectral radiometer (DISR) and visual infrared mapping spectrometer (VIMS) instruments of the Cassini–Huygens mission, but not before 2004.

From the Earth, imaging Titan is a difficult task due to its small angular diameter which is similar to the limit of observing in very good conditions (0.8 arcsec), so that Titan cannot be spatially resolved even from the best observing sites. There are two ways to overcome these limitations: either by using the Hubble Space Telescope (in the 0.9- and 1.1-$\mu$m windows only, at the time of observations) or by means of adaptive optics associated with a large ground-based telescope in the 1.3–2.5-$\mu$m range, where adaptive optics is the most efficient and where contrast of hypothetical surface features is expected to be maximum (other techniques of correction of the atmospheric seeing are less efficient in terms of signal-to-noise ratio). A first resolved image of Titan's surface by means of adaptive optics (Saint-Pé *et al.* 1993) and a test image with the HST wide-field planetary camera (Smith and Lemmon 1993) have confirmed these possibilities of resolving Titan's surface features.

In this paper, we will report results obtained at ground with adaptive optics (AO). Since AO is a new technique, at the highest efficiency level of modern optics, it should be useful to describe in some detail:

—The purpose of adaptive optics, the way it works, and the more recent functionalities of the used instrument (Section 2) ;

—The observing strategy (Section 3);

—The results from raw data at first processed-level (Section 4);

—The final data processing steps (Section 5);

—The final results of the reported observations (Section 6);

—The significance of these results for our understanding of Titan physics (Section 7).

## 2. ADAPTIVE OPTICS

The purpose of adaptive optics (AO) is to compensate in real time the distortions of the incident wavefront which are induced by atmospheric turbulence and thus to produce nearly diffraction-limited images. The Space Research Department of Paris Observatory (DESPA) has developed in collaboration with French companies, for the European Southern Observatory, the first adaptive optics system devoted to astronomy and open to the scientific community as a facility (COME-ON, upgraded to COME-ON PLUS, and now ADONIS). The description of the system is given in Rigaut *et al.* (1991) and Saint-Pé *et al.* (1993). The improvements implemented recently in ADONIS are described by Gendron and Léna (1994, 1995).

The principles of adaptive optics have been proposed by Babcock (1953). The incident wavefront coming from a stellar source does not remain planar when propagating through the atmosphere due to the phase perturbations induced by atmospheric turbulence. As a result the ''seeing-disk'' formed at the telescope focus is much larger than the Airy diffraction pattern and is very unstable. In an adaptive optics system the wavefront distortions are measured continuously. Then phase corrections, opposite to the measured distortions, are applied in the optical path. In practice, the main mirror is reimaged onto a small and very thin deformable mirror acting as a phase corrector. The light beam is divided in two parts, one to determine the phase distortions by use of a wavefront analyzer and the other to form the corrected image. The atmospheric turbulence is basically characterized by a geometrical parameter: the length of coherence (some decimeters) and by the coherence time constant (some milliseconds) which

depend on the wavelength in such a way that adaptive corrections are now quite effective in the near-infrared but not in the visible spectral range. One can take advantage of the fact that the atmospheric disturbances are nearly independent of the wavelength (Roddier and Léna 1984) and use the visible spectral range for probing the phase distortions.

The ADONIS system is formed with a Shack–Hartmann wavefront sensor which characterizes the departure of the actual wavefront from an ideal plan in a set of discrete points into the pupil. The deformable mirror, the phase-corrector, is then actuated by linear piezo-electric motors in order to produce inverse departures in discrete conjugated points. An alternative solution has been proposed by Roddier *et al.* (1988) based on the sensing of local curvatures of the wavefront and their compensation by local curvatures of the deformable mirror. Such systems are now in use in Hawaii at the Univ. of Hawaii Telescope and at the 3.6-m Canadian French Hawaiian Telescope.

It is possible to maximize the spatial resolution of images obtained by means of AO thanks to *a posteriori* deconvolution by a reference point spread function (PSF), usually obtained by recording images of a reference star.

Observations of Titan were performed using the ''modal control optimization'' functionality of ADONIS (Gendron and Léna 1994, 1995). This functionality allows one to recover the best possible image by optimizing the spatial and temporal parameters of the servo-loop correction of the AO system in terms of the observing conditions. One can roughly describe this functionality as follows: the modal control allows to discriminate the different spatial scales in the phase disturbances by use of a set of $N$ spatial modes for the wavefront correction. The advantage of such a control is to allow the correction of only some of these modes judiciously chosen, i.e., the modes with sufficiently high signal-to-noise ratio and sufficiently long correlation time. Specific observing conditions (seeing value, correlation time, and flux from the reference source) correspond to a specific tuning of the AO system.

This also leads to a specific PSF being associated with each new modal optimization. For this reason, special attention was devoted to the use of the same optimized tuning on Titan and on the PSF calibration star. The turbulence is not stationary, and changes in the seeing and correlation speed are unpredictable. During the observations, the turbulence was monitored to search for eventual changes in correlation time and seeing conditions. When necessary, a new optimization was performed.

The only way to ensure that the PSF on the calibration star is as similar to as possible the PSF of Titan is to alternate the observations of the two targets at the highest possible rate. This is the procedure we recommend for any observation with adaptive optics. The method has been successfully employed during the reported run and has led to pairs of observations (Titan–PSF) well suited for deconvolution.

## 3. OBSERVING PROCEDURES

### *3.1. Sampling and Timing*

We have observed Titan near Greatest Eastern Elongation, at the 3.6-m telescope of ESO, from September 15 to September 19, 1994 with an infrared camera adapted to the COME-ON PLUS system, provided by MPI–Garching. The detector is a Rockwell 256 × 256 HgCdTe array (1–2.5 $\mu$m). The read-out noise is negligible with respect to the photon noise and other sources of uncertainty in the conditions of observation. On the other hand, the read-out electronics produces a periodical fixed-pattern noise, the so-called ''correlated noise.'' The linear scale is 0.05 arcsec per pixel which is sufficient for sampling the diffraction pattern (0.11 arcsec FWHM at 1.6 $\mu$m).

In view of achieving the best possible spatial resolution, the recording of sets of short exposure time pictures, which was made feasible thanks to the negligible level of the read-out noise, was preferred to the recording of a small number of long-exposure-time images.

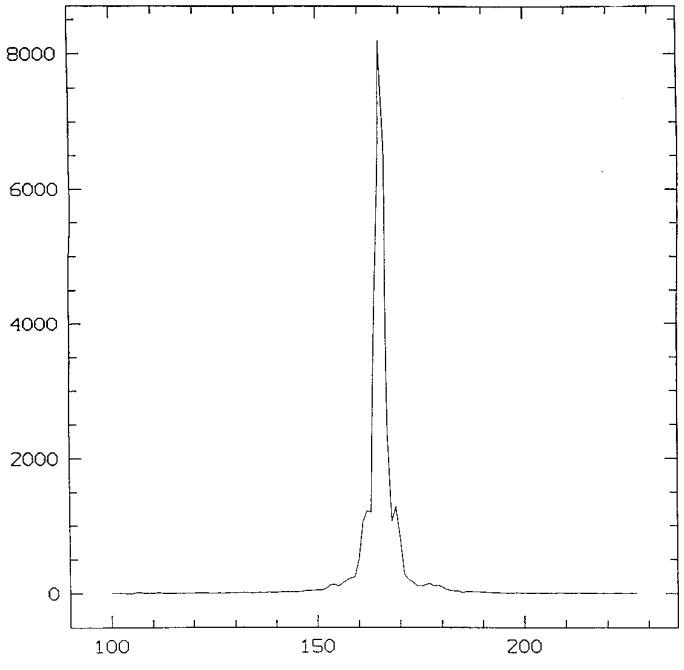


**FIG. 1.** Typical point spread function (PSF) acquired by recording a stellar source in the close vicinity of Titan and in the same conditions as the Titan frames (filter K1, exposure time, etc.) for each Titan's image acquisition. The units on the $x$ axis are pixels, with a sampling of 0.05 arcsec/pixel. The FWHM is 0.14 arcsec at 2.0 $\mu$m, very close to the diffraction limit. Notice the high degree of symmetry in the PSF, showing that the fixed optical aberrations are well corrected by the adaptive optics system. The very high signal-to-noise ratio achieved in the PSF allows for a very efficient *a posteriori* deconvolution to be applied.

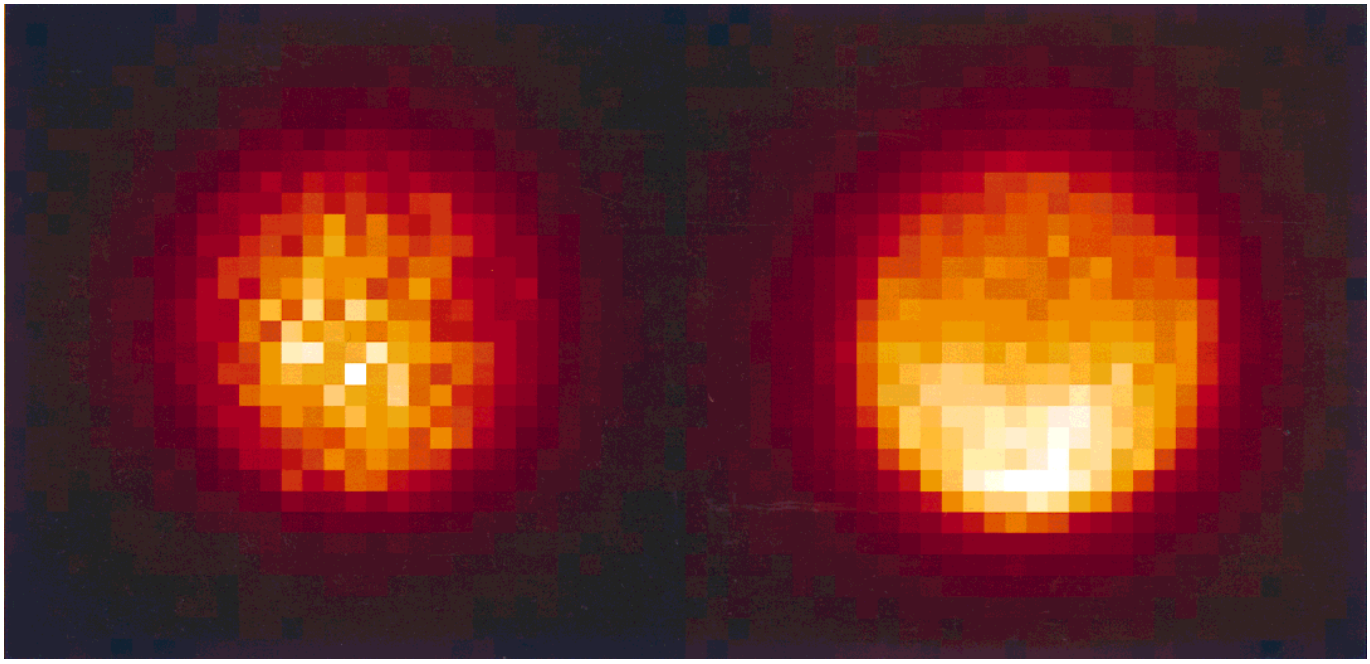

**FIG. 2.** Titan observed in the K1 and K2 narrow-band filters (2.0 and 2.2 $\mu$m) during the night of September 16, 1994. The orbital phase is about 85° LCM (Gr. Eastern Elongation: leading side). The images are processed at first level: the bad pixels and correlated noise have been removed, and the sky contribution and flat-fielding effects corrected for. The spatial resolution on these images is diffraction limited (0.14 and 0.15 arcsec at 2.0 and 2.2 $\mu$m, respectively) with a sampling of 0.05 arcsec/pixel. The two images are different already at this stage (see text). The relative intensities of the two images are not comparable. North is always in the upper side of our images in this and subsequent figures and East is on the right.

### *3.2. Filters*

We used a set of narrow-band filters in the K, H, and J bands (2.0, 1.6, and 1.28 $\mu$m). Specific filters have been defined (K1, H1, and J1) in order to maximize the contribution of the light reflected by Titan's surface into the total signal recorded at the center of the 2.0, 1.6, and 1.28-$\mu$m transparency windows of Titan's atmosphere. In K1, the contribution of the surface is expected to reach 30% of the total outgoing flux while the scattering optical depth is less than 0.1. As a consequence of this low scattering optical depth, surface features, if any, could be imaged without suffering an important degradation in contrast, but the signal is quite faint due to the slope of the solar spectrum. In H1 and J1, the recorded flux is larger by an order of magnitude but the contribution from the ground is not expected to be, in percentage, as large as in K1, and some contrast decrease could be experienced due to an expected scattering optical depth of 0.3–1.0. These estimated values are derived from the definition phase of the DISR instrument of the Cassini–Huygens mission (Tomasko *et al.* 1984) and from more recent studies (McKay *et al.* 1989, Toon *et al.* 1992, Griffith 1993). In all filters, the major contribution is due to scattering in the middle and lower atmosphere. If they exist, large tropospheric cloud structures would thus be observed in this part of the atmosphere which, in any case, is responsible for global center-to-limb variations. A small but significant part of the signal recorded in these filters is due to the stratosphere, resulting from backscattering by the stratospheric haze which is known to have a nonuniform but smooth distribution over Titan's disk and which is thus expected to reduce the apparent contrast of the expected surface structures. For removing this stratospheric contribution in the images, in order to improve the visibility of ground features, images have been recorded in adjacent narrow-band filters (K2, H2, J2) in the wings of the strong methane bands, where the outgoing flux is entirely due to the stratosphere. The wavelength difference between bands-1 and bands-2 is assumed to be sufficiently small as to have a negligible effect on the scattering properties of the stratosphere (this is confirmed by a large similarity between our H2 and K2 images, as it will be discussed later). Images in bands-2 have been recorded for every bands-1 set of observations.

### *3.3. The Observational Strategy*

The image of Titan is focused onto one of the four adjacent quadrants (frames) forming the IR detector array. Then the servo-control of the adaptive optics is activated. Some tens of exposures (10 to 40 in most cases) with an elementary exposure time of some seconds (e.g., 2 sec in K1 and 10 sec in K2) are achieved and independently recorded in the computer memory. Then an ''on–off'' mir-

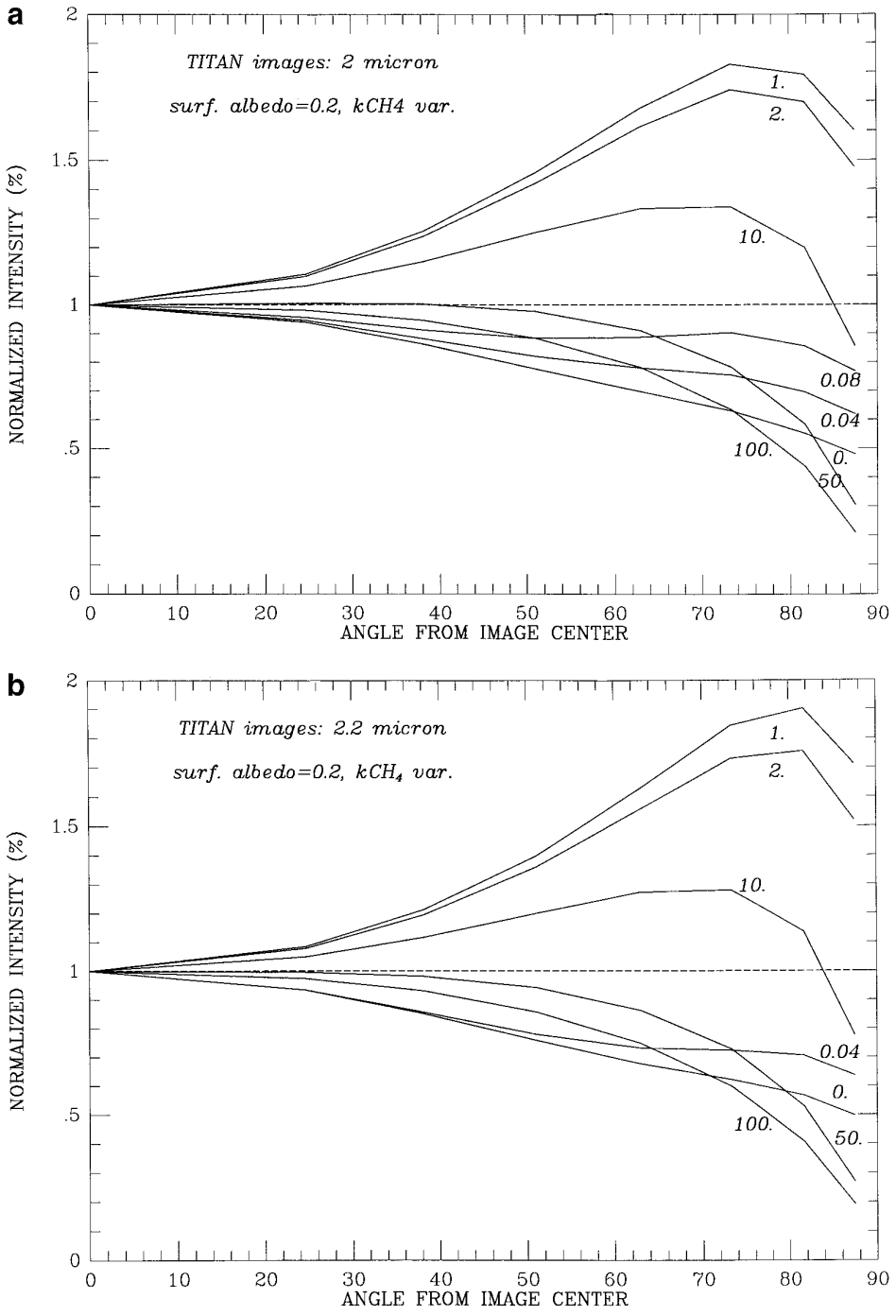


**FIG. 3.** Examples of calculated normalized intensities as a function of the angle from the image center using McKay *et al.* (1989, adapted) radiative transfer code (with the cloud optical depth, the surface albedo, and the methane absorption coefficients as parameters) at (a) 2 and (b) 2.2 $\mu$m to correct for center-to-limb effects on our deconvoluted images.

ror translates the image of Titan onto another quadrant of the detector. A new set of recordings is achieved with the same parameters (filter, exposure time, number of exposures). This cycle is repeated at least twice.

This observing procedure presents several advantages. During the recording of a Titan image, the sky brightness is recorded simultaneously on the adjacent quadrant where the image of Titan will be moved by the on–off technique and vice-versa. As a result, the sky contribution, which may vary quite rapidly in the near IR, is efficiently measured by

this interweaving method and can easily be subtracted from the images. The elementary exposures are then coadded and the basic cycle of observation results into two *elementary images* of Titan onto two different parts of the IR detector array. Thus, these two elementary images cannot suffer from identical distortions resulting from hypothetical incomplete or erroneous corrections of the pixel-to-pixel sensitivity variations in the flat-fielding process. As a consequence, similarities of observed common morphological details on these two images are undoubtedly highly significant.

We then record an image of a star, at a short angular distance from Titan, of the same brightness and close to the solar stellar type, with the same sequence of observations, with similar exposure time, and in the same filter. The use of these stellar images as point spread functions should lead to further improvement of the spatial resolution by means of an *a posteriori* deconvolution process, provided sufficiently high signal-to-noise ratios are available.

The complete sequence can be repeated identically or through another filter. Using this observational approach, the total observing time was 4 to 5 hr per night centered around Titan's culmination.

### 3.4. Flat Fielding

Flat fields can be obtained by two different methods. The first method is by imaging the bright sky at zenith before twilight with 30- to 60-sec exposure times in the different filters. The dark current pattern must be recorded during the same exposure time in order to avoid any nonlinear effect. Another method is to add all the elementary observations excluding the quadrants where Titan or a star were recorded. This requires the recording of a set of dark current patterns with the same elementary exposure times.

### 3.5. Reduction and Processing of the Data

The elementary images are processed in the usual way. Dead pixels and cosmic impact traces are eliminated, the fixed noise pattern is filtered by Fourier Transform, and a flat-field correction is applied. Then these ''first-level processed'' images are deconvoluted by the corresponding PSF which have also been first-level processed. In a subsequent step, center-to-limb effects are removed from the deconvoluted images from models. Finally, the stratospheric haze contribution is subtracted from the band-1 images using the band-2 data. The steps of this processing will be discussed in more detail in Section 5.

Hereafter we concentrate on our 2.0- and 2.2-$\mu$m images only.

## 4. RESULTS FROM RAW DATA AT FIRST-PROCESSED LEVEL

Because we report on new data resulting from advanced optics that use high-technology IR detectors and sophisticated data processing, we shall first present and discuss intermediate results (prior to any sophisticated treatment).

### 4.1. Flat-Fields

The search for surface features at a contrast level from a few percent to 30% at most and with subarcsec size implies determination of the pixel-to-pixel sensitivity variations on the detector array at an even higher level of accuracy.

The observing and data reduction procedures lead to one sensitivity map per observing night. We have thus obtained, in 1994, four independent maps. We can estimate the accuracy of these maps from a statistical analysis of the differences between two independent maps. The mean value of such a difference must be zero and the value of a given pixel is related to the errors on the determination of the true value of the pixel sensitivity and to the quadratic addition of the photon noise. The mean accuracy of the sensitivity map may be estimated from the histograms of all the pixel values obtained for the differences of two independent maps. Such histograms can be built for the set of sensitivity maps differences. As a result, these histograms are highly symmetrical with very similar r.m.s., so that it seems reasonable to define an ''optimal flat field'' from the mean of the four sensitivity maps. The final uncertainty on the sensitivity of a pixel is then about 2%.

It is also of interest to analyze the statistical spatial distribution of the sensitivity uncertainties onto the detector in order to ensure that any observed features on Titan's images cannot be due to spots of adjacent poorly corrected pixels. Isophots of the differences of independent sensitivity maps show that such an occurrence is very unlikely.

In conclusion, we find the sensitivity map of the detector to be defined with a mean accuracy of 2% or better and that aggregates of erroneously corrected pixels exceeding a unique pixel in size and 3–4% in contrast, are very improbable. In reality, this conclusion is very conservative since every first-level processed image of Titan is formed from a couple of images recorded onto two different quadrants of the detector which cannot suffer similar poor corrections, if any, of flat-fielding defects and since, moreover, the successive Titan images were slightly shifted on the detector.

### 4.2. First-Level Processed Images

The observations were scheduled during five consecutive nights. The second night was lost due to weather conditions. The real-time correction provided by the adaptive optics was very efficient. We have obtained images, for most of the 1994 observing run, with Strehl ratios ranging from 0.2 to 0.6 without *a posteriori* deconvolution. (Let it be reminded that the Strehl ratio is the intensity at the peak of the actual seeing disk of a star divided by the

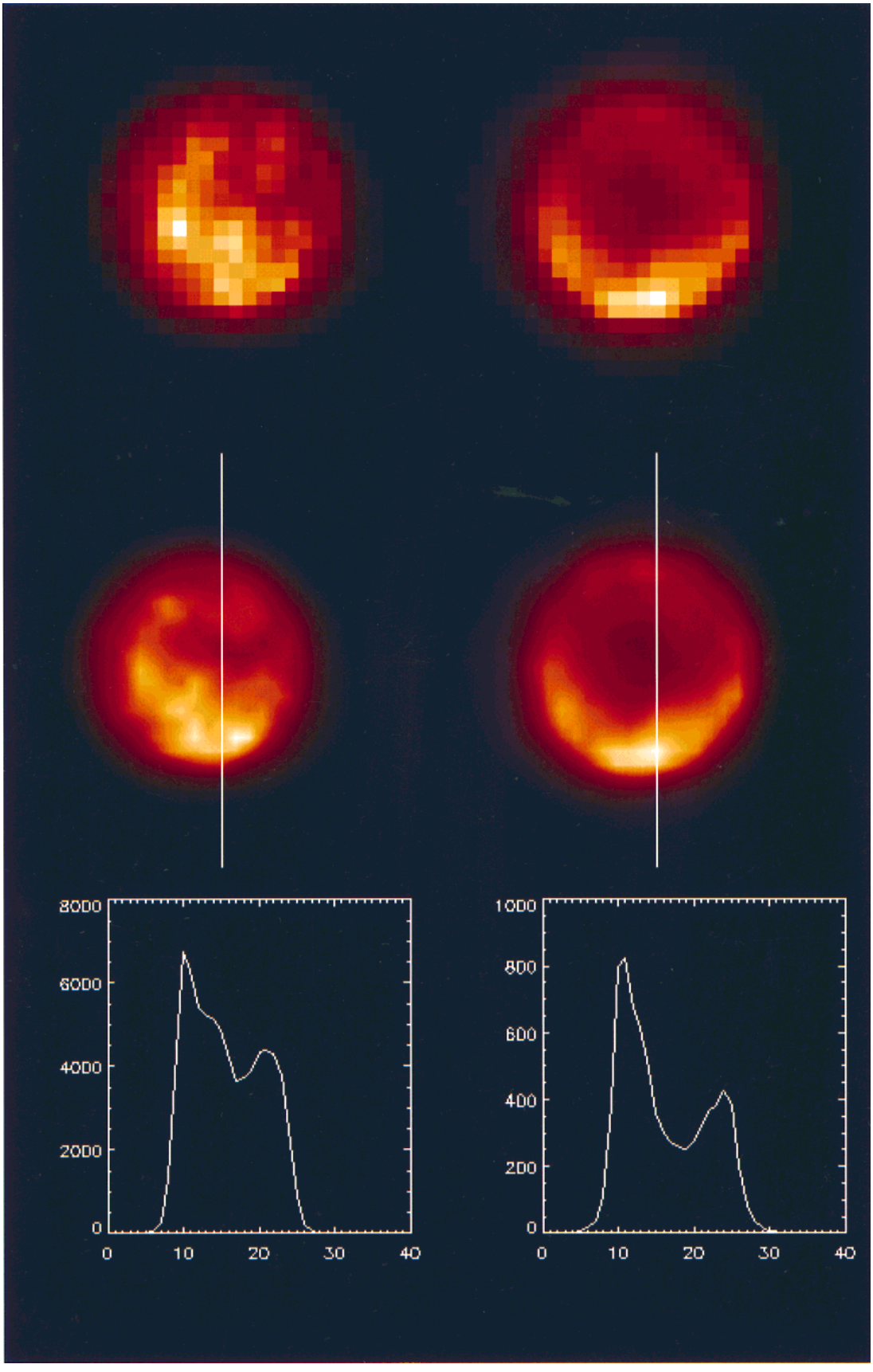
8000
6000
4000
2000
0
0
10
20
30
40
1000
800
600
400
200
0
0
10
20
30
40

intensity at the peak of the ideal Airy diffraction pattern. In a very good observing site the nominal Strehl ratio is usually less than 0.05, even in the near infrared (Babcock 1990).) Figure 1 shows a typical PSF. Its sharpness is remarkable. Its high level of symmetry indicates that the fixed optical aberrations of the telescope and associated optics are well compensated. As a consequence *first-level processed* Titan images are fully significant by themselves even before deconvolution, and it may be useful to present and discuss briefly these images in order to have a basis for comparison with further final-processed deconvoluted images.

The K2 images of Titan processed at first level before deconvolution are already characterized by a large hemispherical asymmetry. The southern hemisphere is brighter than the northern by 20–30% (Fig. 2). The bright zone extends closer to the equator toward the western limb. A dark spot can be seen in the northeast part of the frame. The time dependence of the morphology in the K2 spectral band is faint as deduced from 1993 and 1994 images comparison. At a day-to-day rate, the stratospheric morphology appears to be very stable. The north–south asymmetry inversion with respect to Voyager 1 observations was expected, as recalled previously.

The K1 images of Titan differ significantly from the K2 images. A bright region can be observed, even at this first-level processing step, close to the equator, centered at a latitude of 13° south and at a longitude close to 114° (Fig. 2). Some fainter bright features can be observed in the SW and in the northern hemisphere. There is no need to describe these features in more details at this level, our purpose being only to have a comparison basis for discussing the final deconvoluted images. It may be noticed that this bright feature and the associated features can be seen on every set of images and that over three consecutive nights the displacement of this bright spot is quite similar to what would be expected from the rotation period of Titan even before corrections of center-to-limb effects. This bright feature has been attributed to actual variations of Titan's surface albedo (Combes *et al.* 1995a, 1995b, 1996a, 1996b).

## 5. COMPLETE DATA PROCESSING

### *5.1. Deconvolution*

Due to the effectiveness of the AO, the PSFs are very sharp, and due to the significant observing time that was possible to devote to stellar images, the signal-to-noise ratios on the PSFs are very high, so that an *a posteriori* deconvolution of the first-level processed images is expected to be efficient.

Using the deconvolution methods described here, we have obtained statistically reasonable solutions to the deconvolution problem in adaptive optics. Our analysis is based on some hypotheses, which are not always satisfied, but we have applied a number of independent methods giving the same results, which reinforces the credibility of our findings. In the subsequent figures, we have plotted the results of the deconvolution method of maximum entropy, unless otherwise indicated. All methods give, however, coherent and quite similar results. We hereafter briefly describe the deconvolution methods used with our data and which are contained in the IDOLA package especially developed for the reduction and analysis of the ADONIS adaptive optics data (information on IDOLA is available on www.despa.obspm.fr).

The first two methods applied on our data set are basic deconvolution procedures such as inverse filtering and Wiener filtering. Inverse filtering can be used to compute a first approximation of the object. This method is not correct because it assumes that deconvolution is a linear problem (which is, of course, not true) and because it does not account for the stochastic characteristics of the signal. In practice, this method magnifies the noise in the restored image, but the result can be improved using a low-pass filter. Because this is a noniterative deconvolution method, a restored image can be rapidly obtained. The Wiener filtering method minimizes, in a least-mean-square sense, the difference between the mathematic expectation of the solution and the restored image. It is a noniterative deconvolution method, so it is rapid. Wiener filtering requires some knowledge of the spectral density of the real object and it assumes that the image has been perturbed by an additive gaussian white noise (it is possible to demonstrate that Wiener filtering is theoretically correct in the case of a signal-dependent noise, like photonic noise: see for example Kondo *et al.* 1977). We have used the simplest method to obtain a restored image using Wiener filtering, which consists of replacing the spectral density of the object by a constant value (so we assume that the signal is white) and in adjusting it. If we choose a small value for this constant the high frequencies will be underestimated in

**FIG. 4.** Same as Fig. 2 but fully processed images. These images were deconvoluted by the associated PSF using the maximum entropy method and compensated for the center-to-limb effects. Note the hemispheric asymmetry in the K2 image (more sensitive to the atmospheric contribution than K1 because taken in the methane band), and in particular the bright south limb in the K2 image (probably due to a strong aerosol concentration in this area—see text). The K1 image (corresponding to the center of the 2.0 atmospheric window) allows us to probe deeper into the atmosphere and surface and exhibits an additional bright feature near the equator. Also shown is Titan's surface at 2.0 and 2.2 $\mu$m obtained by smoothing the K1 and K2 images of the previous figure. The vertical cut performed on this images shows the contrast achieved to be about 30%.

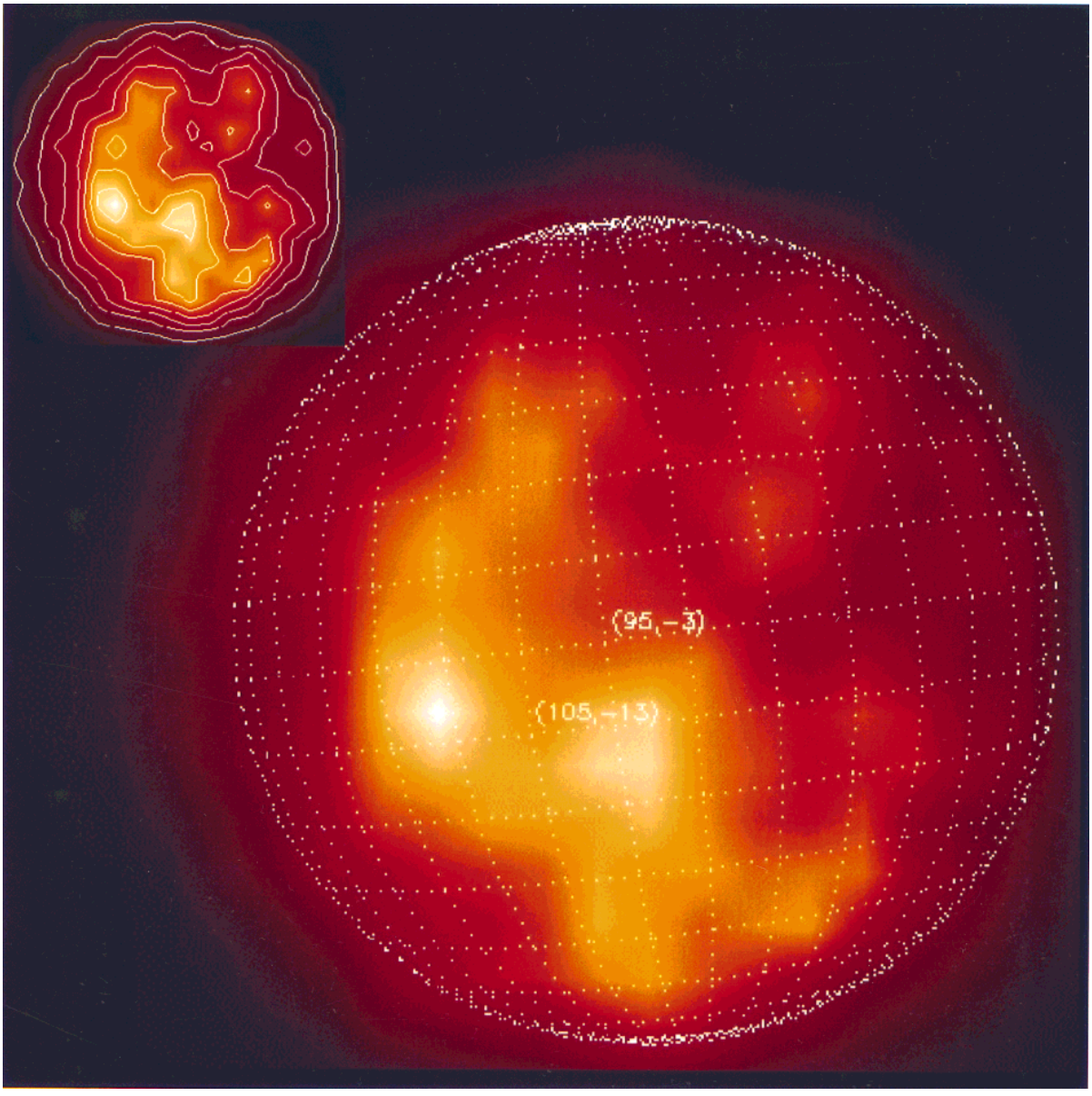


**FIG. 5.** Projection of Titan's surface at 2 $\mu$m on the leading side (16 September 1994), showing the equatorial bright spot centered near 13°S and 114°LCM. It extends over about 30° in latitude and 60° in longitude. The spot is resolved here for the first time into several individual poles. Other bright spots are visible in the SW region (near 25°S) and in the northern region (near 30°N). Also shown are isophots indicating the presence of several distinct independant centers inside the resolved bright equatorial region.

the restored image and the method will magnify the noise. The Wiener filtering method seems to be a reasonable and quick solution to the deconvolution problem, but the restored images have poor resolution.

The more sophisticated and iterative methods applied on our data include the Richardson–Lucy (maximum likelihood) and the maximum entropy methods. The Richardson–Lucy is an iterative deconvolution algorithm based on the maximum likelihood principle. It consists in choosing the distribution of intensities which have the maximum probability to have generated the data. This method converges toward the most likely solution (in the maximum likelihood sense). It is a very attractive method because it preserves the global flux and the positivity of the image and it is relatively resistant to noise. However it is somewhat slow because it requires two convolutions (four Fourier transforms) per iteration. In order to improve the convergence of the algorithm, we have used a regularization method (Starck *et al.* 1994). The regularization for an additive signal-independent gaussian white noise is based

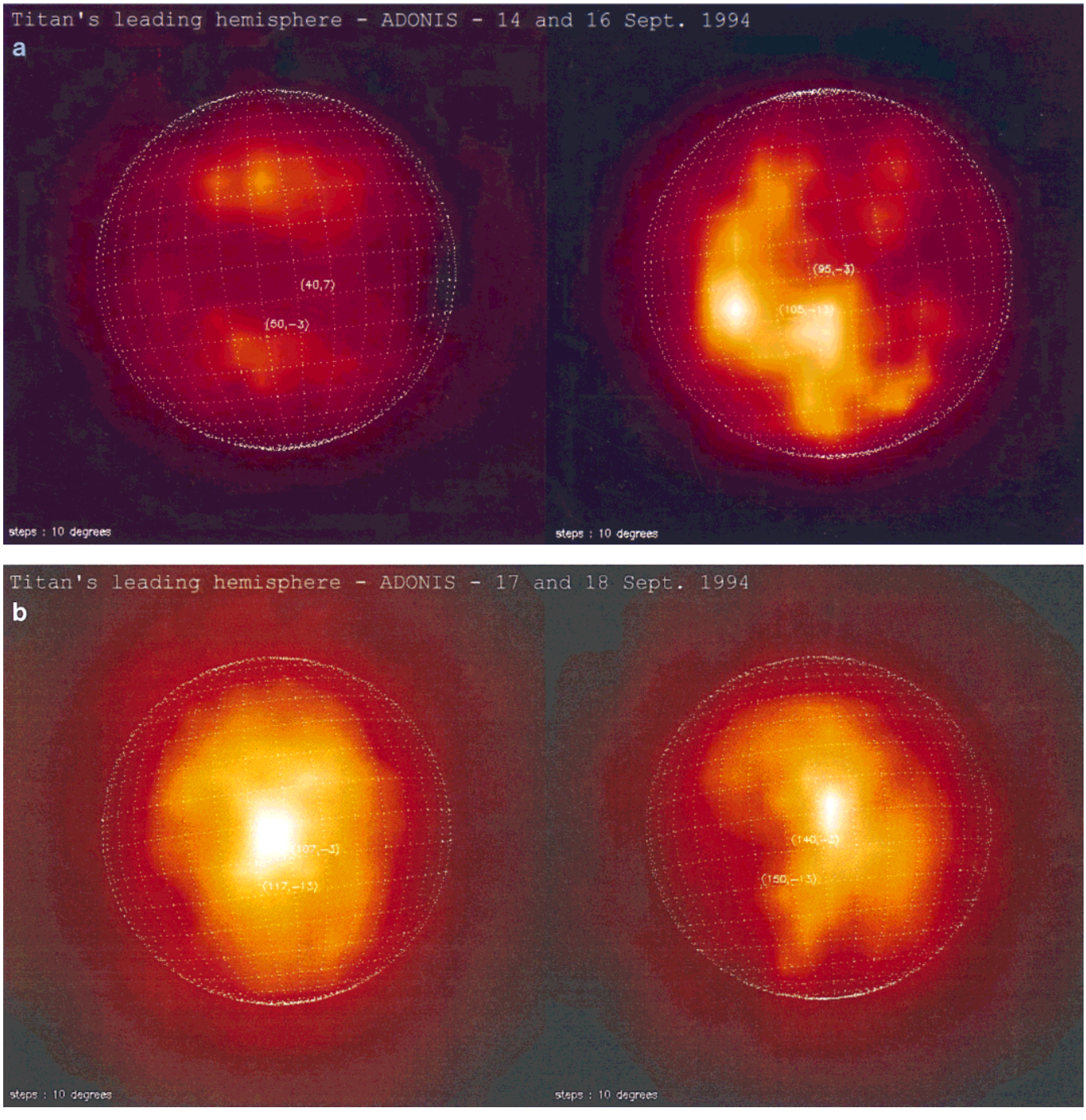


**FIG. 6.** Titan's surface on the leading hemisphere from 1994 images taken near Gr. Eastern Elongation on 4 out of 5 consequent nights: (a) September 14 and 16 and (b) September 17 and 18. Note the pronounced bright region near the equator on the night of September 16 and afterwards, moving at the rate expected for a synchronous rotation of Titan from west to east (left to right). On the first night the bright spot is not visible yet and a north–south morphology can be observed, similar to that found on the trailing side in 1995 data (Fig. 8).

on the so-called ''à trous'' wavelet transform. It consists of a $3\sigma_k$ clipping ($\sigma_k$ is the standard deviation of the noise at scale $k$) in the different frequency planes of the wavelet transform of the residual computed at each iteration. For more precisions, see Starck and Murtagh (1993). The maximum entropy method (MEM) algorithm follows from a Baysian approach of the deconvolution problem. MEM supposes that the most likely solution, taking into account

the positivity and the finite support constraints, is the one which has the maximum entropy (the entropy gives an idea of the amount of information). The method converges toward the estimation which minimizes a data connection function and a parameter of regularization. Usually, the images restored with MEM have better resolution than those obtained with the Richardson–Lucy algorithm.

### 5.2. Modeling of the Haze and Center-to-Limb Effects

We have used the McKay *et al.* (1989) radiative transfer code which includes scattering and computes Titan's geometric albedo. Given a nominal methane absorption coefficient for each wavelength ($k_{CH4}$) taken from laboratory measurements (Strong *et al.* 1993), Coustenis *et al.* (1995) have inferred Titan's surface albedos deduced from geometric albedo values resulting from CFHT Fourier transform spectrographic data taken since 1991. The atmosphere as a whole can have a positive or a negative contribution to the total backscattered flux. In the Lambertian approximation, the surface albedo is equal to 3/2 times the geometric albedo. The calculations show that the atmosphere lowers the total albedo at 1.3 $\mu$m and increases it at other wavelengths for the nominal values of $k_{CH4}$.

The surface albedo values are then used to model limb effects (with an adapted version of the McKay *et al.* code) on the Titan images in terms of the radiance expected as a function of the angle from the center of the image (Figs. 3a and 3b). We use the surface albedo, the $k_{CH4}$, and the haze production rate as parameters and derive the expected limb effect, and then we correct for it on the deconvoluted images.

### 5.3. Atmospheric Contribution Subtraction

As mentioned previously, a small but significant contribution to the K1 images is due to the stratospheric haze. This contribution is removed by subtracting, from the K1 images, a component proportional to the K2 images which are entirely due to the stratospheric backscattered flux. We assume that the difference in wavelength (nearly 0.1 $\mu$m) between K1 and K2 has a negligible effect on the absorbing and scattering properties of the haze. The similarity between K2 and H2 images (Combes *et al.* 1997) tends to support this assumption.

An estimate of the proportionality coefficient $f$ is achieved by taking into account, for both bands, the ratios of the transmissions of the filters, the Earth atmospheric transmissions, the incoming solar fluxes, the transmissions of Titan's stratosphere above the level of the haze, and the exposure times. The first term can be deduced from calibration data of the filters. The Earth transmissions and solar fluxes are taken from the literature. They are close to unity. The ratio of the stratospheric transmissions is more important due to the difference in methane absorptions; it is estimated from the model used in Section 5.2. The model is admittedly subject to uncertainties because, for one thing, the haze is assumed to be constant with latitude which is evidently not the case. The nominal ratio value was found to be 3.85. The ratio of the exposure times is accurately known.

For exposure times of 2 sec in K1 and 10 sec in K2, the value of $f$ is estimated to be 2.8 with an uncertainty of $\pm 20\%$. Practically, varying $f$ from 2.25 to 3.75 results in a variation in the contrast of the observed surface features but does not affect their positions nor their shapes. The practical solution used here is the simplest and best way that we are aware of for removing haze effects from the K1 image.

This procedure allows subtraction of the stratospheric haze, but no more. The resulting (K1 $- f \times$ K2) images contain the contribution of deep haze (which is not probed in K2 due to the methane absorption), the contribution of the low atmosphere and in particular of tropospheric clouds, if they exist, and of surface structures. The way to discriminate between the altitudes of observed morphological structures is to observe their time evolution: clearly the surface features will move, from night to night, at the rate of the rotation period of the planetary body. The tropospheric wind velocity is expected to be large enough to induce discernible displacements with respect to the solid body rotation within one or two consecutive nights. The high-altitude wind velocity is expected to be much larger.

## 6. RESULTS

The K1 and K2 deconvoluted images (Fig. 4) are entirely consistent with the first-level processed images with, as expected, more resolved and accentuated morphological details, which were only suspected at the first-level processing, but without ''unexpected'' subtle new features introduced. This fact tends to support the conclusion that the used deconvolution procedure, thanks to the high signal-to-noise ratios of our image, does not introduce artifacts. As an expected result of the deconvolution process, the contrast of the surface marks is increased and reaches 30%.

The deconvoluted images exhibit a limb-darkening consistent with our modeling at these wavelengths which predicts a 10–20% limb darkening for emission angles larger than 50° in K2, where the methane absorption is large (about 70 (km-Am)$^{-1}$, Strong *et al.* 1993) and a very slight limb-darkening in K1, where the methane absorption is low (about 0.04 (km-Am)$^{-1}$), as explained in 5.2. It is then justified that the center-to-limb effects have been indeed compensated with this modeling. Note however that the correction is not perfect since the methane abundance, as well as the haze altitude and latitudinal distribution, are not well known and assumed to be constant in our model.

The final subtracted (K1 $- f \times$ K2) images of the leading hemisphere show a well-defined equatorial bright spot associated with smaller and fainter features at high latitudes in both hemispheres forming an extended bright region surrounded by a dark zone (Fig. 5). Furthermore, the bright equatorial feature is spatially resolved in three marks. All of these spots are rotating at the expected rotation rate of Titan's solid body with an accuracy better than one pixel over consecutive nights, which is better than the detection limit of the instrument. So they can be definitely attributed to ground features (Fig. 6a and 6b).

Our images are in good agreement both on the location and the global shape of the bright feature with HST images (Smith *et al.* 1996) obtained also in Titan's atmospheric transparent windows at 0.94 and 1.08 $\mu$m (Fig. 7). As expected from the scattering properties of the atmosphere and its aerosols the contrast of the observed surface spots is higher in our near-IR images (about 30%) than in HST images (about 10%). The spatial resolution of the HST undeconvoluted images at 1 $\mu$m obtained with a 2.4-m telescope is similar to the resolution of our deconvoluted images obtained at 2 $\mu$m with a 3.6-m telescope. Most importantly, these two entirely independent observational sets are in very good agreement, firmly establishing the reality of the observed surface features.

Two differences, not divergences, between HST and ADONIS images can be noted:

• The equatorial bright spot is spatially resolved into several ''peaks'' in our deconvoluted images. This might be due to the higher contrast achieved at 2 $\mu$m (Fig. 5);

• The images of Titan's trailing side are mainly featureless in HST observations. In the 1995 ADONIS data, they show a significant north–south asymmetry, after removing the stratospheric contribution (Fig. 8). A bright region can be observed at high northern latitudes (>40°N) on Titan's surface and a dimmer bright region seems also present at high southern latitudes (>30°S). The zonal bright regions are also observed in our 1994 images of the leading side on the first observing night when the equatorial bright spot is not yet observable, or on the following nights if the bright spot is ''masked'' in the data processing in order to increase contrasts. This north–south feature appears then to be confirmed in the first data reduction of our 1995 images which are related to Titan's trailing hemisphere and in our 1994 leading side images. They do not seem to result from a systematic effect of the data-reduction procedure, and in particular of the K2 images subtraction or of the center-to-limb darkening, since the northern polar zone is the brightest while the southern hemisphere is brighter in K2 and because our model for center-to-limb darkening is fully symmetrical. It is reasonable then, as a preliminary conclusion, to assume that—with the exception of the bright equatorial spot—the near polar regions of Titan's surface are significantly brighter at all longitudes than the dark material covering most of Titan's surface, with the North Pole brighter by about a factor of 2 with respect to the South Pole. This difference with HST images could be due, first, to the large optical depth of Titan's atmosphere at 1 $\mu$m near the limb, impeding the mapping of high-latitude regions, and second (and more importantly), to the data processing procedure applied to the HST images which tends to eliminate zonally symmetric features (Smith *et al.* 1996).

## 7. DISCUSSION

The ADONIS spatially resolved images of Titan presented in this paper, their complete agreement with HST observations by P. Smith and colleagues, and the precise coincidence of the displacement rate of the observed features with the expected rotation period of Titan's solid body lead to the clear conclusion that Titan's surface is undoubtedly heterogeneous. This confirms the interpretation of spatially nonresolved observations from radar or near-infrared photometric and spectroscopic data. The spatially resolved images from ADONIS show that the surface heterogeneity is quite complex. The revealed morphology exhibits further details at the level of the best achievable resolving power and with important albedo contrasts. It appears that the bright regions are concentrated in a basically continuous area surrounded by darker ''terrains'' covering most of Titan's surface. On the other hand, the resolved images presented in this paper show that if the bright region is clearly located in the leading side it is far from covering an entire hemisphere.

The model of a global ocean formed from liquid methane mixed with ethane, other liquid hydrocarbons, and nitrogen, as supported by Lunine *et al.* (1983) and others, based on Voyager data, thermodynamical evidences, and estimated photochemical production rates, must be ruled out. While the theoretical considerations by Sagan and Dermott (1982) relative to the tidal dissipation of the eccentricity of the orbit of Titan, which supported the concept of a ''global'' ocean, were recently revised (Sagan and Dermott 1995), the fact that methane and ethane are liquid at the temperature and pressure conditions of Titan's surface and that a methane reservoir is needed to account for the present state of Titan's atmosphere remain severe constraints for any modeling of this body's surface. These liquid hydrocarbons may be present in large basins or lakes at Titan's surface or be intimately mixed in a porous regolith of ices and organics in a subsurface reservoir. These various possibilities should result in different morphological signatures which might be observed in our resolved images.

Liquid $CH_4$ and $C_2H_6$ are very strong absorbers in the 2.1-$\mu$m region. In principle, the IR flux in this window should be entirely absorbed by liquid hydrocarbons, with the possible exception of liquid hydrocarbons deeply mixed

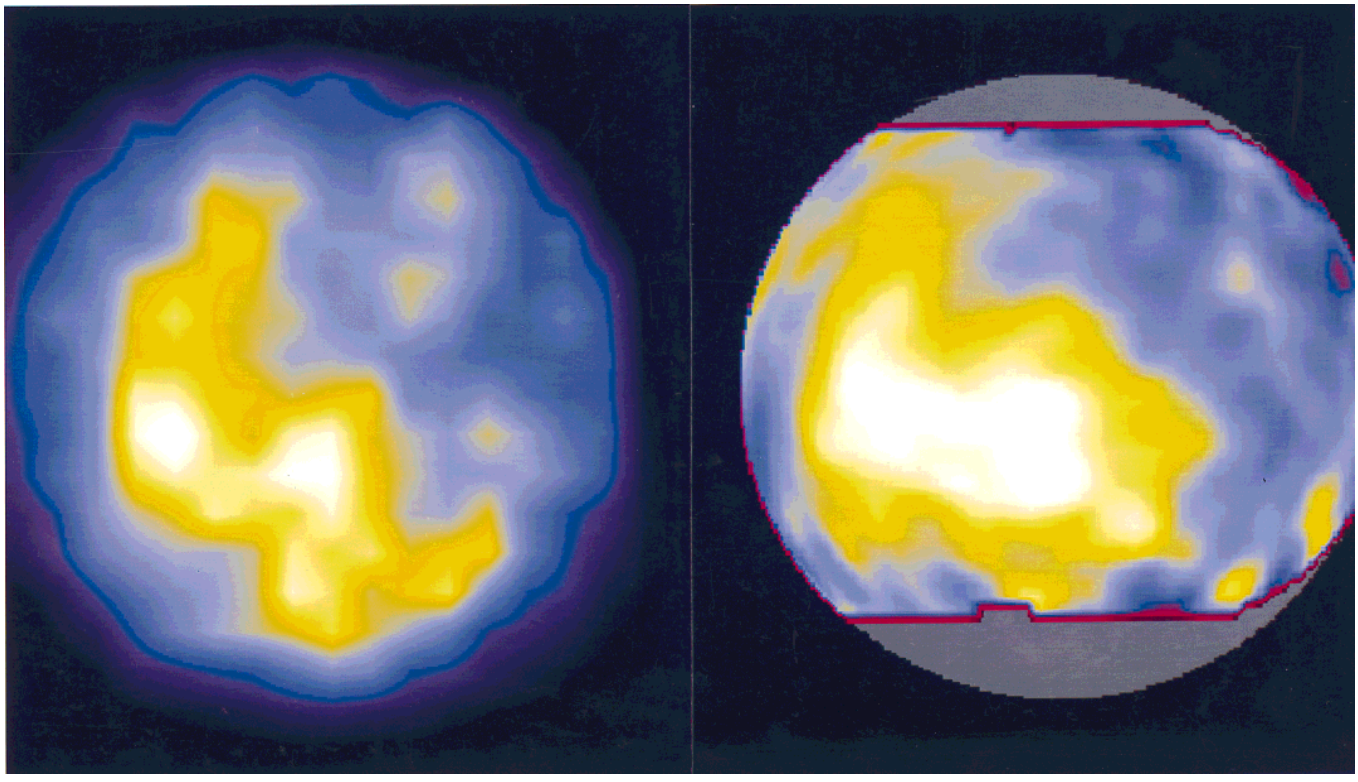

**FIG. 7.** Titan's surface as seen by the HST (right) near 1 $\mu$m (map) and by ADONIS (left) near 2 $\mu$m (1 image) at the same longitude on the leading hemisphere in 1994. Note the excellent agreement between the two observations (The HST image courtesy of P. Smith).

with organic aerosols limiting the penetration of the IR flux, which may not be very different in consistence from a porous regolith. So ''clean'' liquid hydrocarbons basins or lakes should appear as very dark features in our images. Our data do not support the presence of such large structures of free liquid hydrocarbons at Titan's surface on the leading hemisphere even in the ''dark'' regions, which are not so dark when compared to other Solar System objects (Coustenis *et al.* 1995).

The nature of these dark regions is not yet understood. The related albedo is not sufficiently low to be due to liquid hydrocarbon large structures as said before, but is not incompatible with a net of spatially unresolved structures retaining liquid hydrocarbons. The spectroscopic data in the near-infrared range are consistent with the presence of organics like tholins, which would be expected to accumulate on the ground as a result of the photochemical long-term activity of Titan atmosphere, and which are bright and exhibit a flat spectrum in the infrared range of relevance here (Khare *et al*. 1984, Coustenis *et al.* 1995). Furthermore, the near-infrared spectroscopic data suggest that water ice seems to be quite uniformly present on Titan's surface (Coustenis *et al.* 1995). These infrared data could also be consistent with a large coverage of Titan's surface by anhydrous silicates (Coustenis *et al.* 1994) although the uncertainties on the data are too large for a firm identification and the existing models on the origin and evolution of Titan could not easily account for such a large superficial abundance of silicates. Note that the available spatially resolved and spectroscopic infrared data, as well as radar data (Muhleman *et al.* 1995), are not compatible with the presence of a large amount of free liquid hydrocarbons but do not exclude that Titan's surface be basically covered by a hydrated and maybe silicate-covered regolith containing or masking buried liquid hydrocarbons.

The nature of the bright south-to-equator region clearly seen in our spatially resolved images is also poorly understood. Several explanations have been proposed; e.g., icier terrains providing higher albedos, soils washed by methane rainfalls eliminating dark organic deposits, elevated mountains or plateaus appearing brighter due to lower atmospheric absorption, high reflecting tropospheric clouds, chemical species like $CO_2$ or CO ice, or cataclysmic cratering impacts revealing the deep bright subsurface layers. Clearly, our data are not sufficient by themselves to resolve the question.

Nevertheless, we can conclude from our data and from preliminary analysis of resolved images at higher spectroscopic resolution (CVF, $R = 60$), which will be published

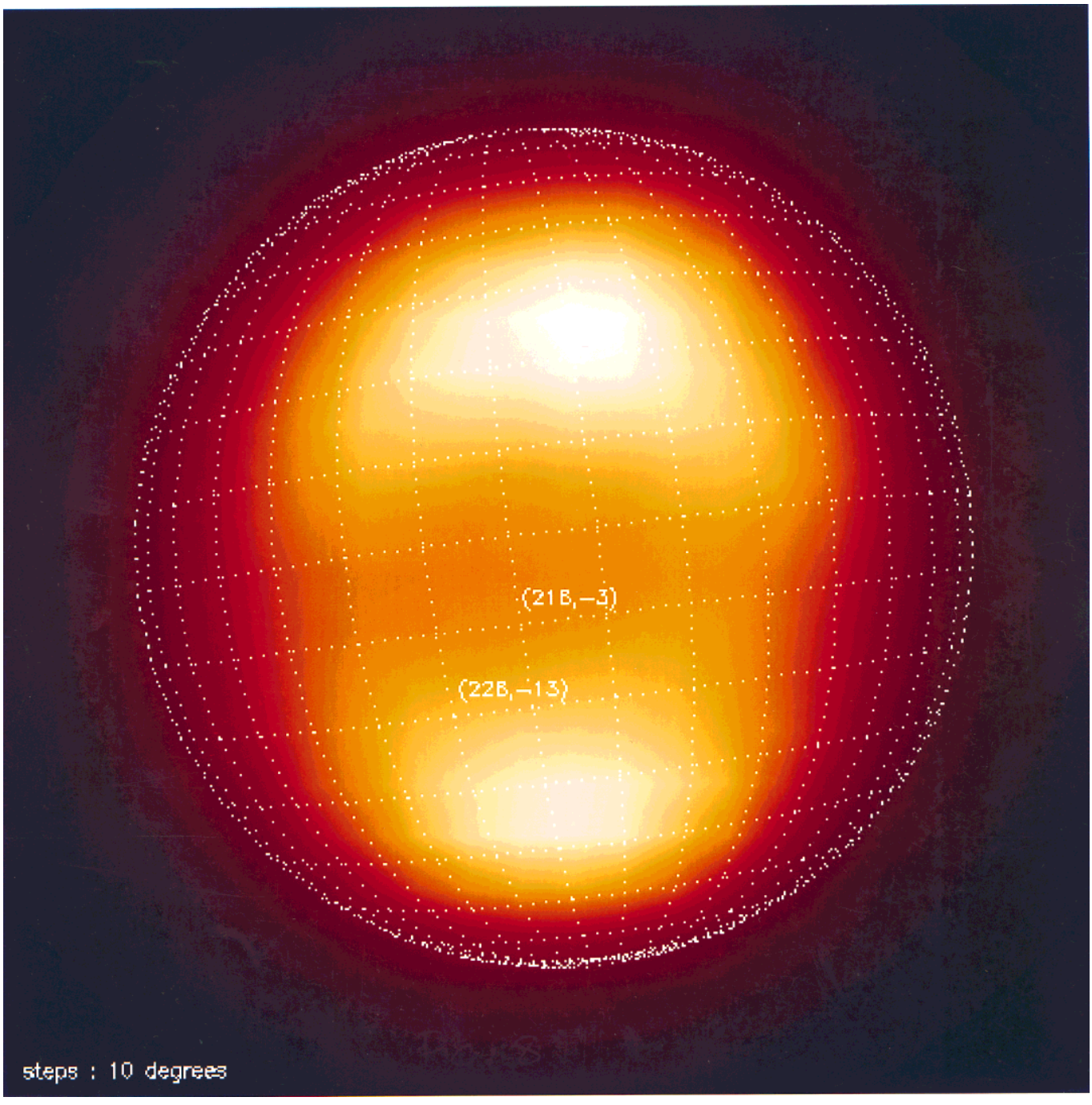


**FIG. 8.** Titan's surface on the trailing hemisphere (Gr. Western Elongation) from 1995 (October 10) images. Note the surface brightness at high northern and southern latitudes, with some north–south asymmetry based on a brighter (factor of about 2) northern region.

in a forthcoming paper, that (a) the observed morphology is very stable with time; (b) there is no evidence for cloud structures, which does not support the probability of frequent rainfalls, (c) the observed albedo contrasts appear unchanged in the $H_2O$, CO and $CO_2$ absorption bands at 2 $\mu$m, which does not favor the hypothesis of icier terrains nor of CO and $CO_2$ ices. Furthermore, Coustenis *et al.* (1997) have shown that even very highly elevated terrains cannot account for the observed data in the lack of simultaneous important additional albedo variations. So there is no obvious explanation of the nature of the bright regions on Titan.

We suggest (in a combined analysis with the results of Coustenis *et al.* 1997) that the morphological structures that we observed and which are quite complex, may be related to terrains locally covered by icy methane (or ethane) which is bright at 2 $\mu$m, and which is plausibly present at temperatures lower than about 90 K, expected for example at the poles or on top of a mountain near the equatorial regions. Another possibility for the polar brightness would be a permanent polar cloud deck (or mist) in the low troposphere, which could be responsible for the polar brightening that we observe, the difference between north and south poles being due to seasonal effects.

## 8. CONCLUSION

Adaptive optics has demonstrated its powerful capability of achieving the full resolving power of 4-m-class ground-based telescopes in the near infrared spectral range. The feasibility of imaging the surface of Titan in transparent atmospheric windows is clearly established. The results of the COME-ON PLUS/ADONIS observing program of Titan are in full agreement with HST observations and are, in some aspects, even more accurate at the present time.

The main results of our program are, at this point, as follows:

• the leading hemisphere of Titan exhibits a large bright region centered at 13° south in latitude and 114° LCM in longitude and extending over about 30° in latitude and about 60° degrees in longitude. This region reveals a complex structure with resolved sharp brighter peaks and albedo contrasts reaching or exceeding 30%;

• the surrounding terrains are darker but not completely featureless;

• a brightening at high northern and southern latitudes existing all over the Titan disk is compatible with our data. The southern ''polar cap'' appears fainter by a factor of about 2.

It must be noted that these results are not strongly dependent on the data reduction methods, nor on the deconvolution processes applied, or on the atmospheric and stratospheric effects correction.

We suggest that the dark regions may be uniformly covered by an icy (and perhaps silicate-covered) regolith material containing or masking liquid methane and other hydrocarbon reservoirs. The bright regions might be mountainous terrains covered by methane (or other hydrocarbons) ice. Frosty methane or polar cloudiness (mist) in the low troposphere may also account for the observed polar brightening.

Additional results, obtained in 1994, 1995, and 1996 in narrow-band filters in J, H, and CVF will be presented in forthcoming papers.

## ACKNOWLEDGMENTS

We thank Chris McKay for adapting and allowing us the use of his radiative transfer code to correct for center-to-limb effects on our images and for fruitful and enlightening discussions. We thank the two referees for very helpful comments.

## REFERENCES

Babcock, H. W. 1953. The possibility of compensating astronomical seeing. *Proc. Astron. Soc. Pacific* **65,** 229.

Babcock, H. W. 1990. Adaptive optics revisited. *Science* **249,** 253–257.

Bézard, B., A. Coustenis, and C. P. McKay 1995. Titan's stratospheric temperature asymmetry: A radiative origin? *Icarus* **113,** 267–276.

Caldwell, J., C. C. Cunningham, D. Antony, H. P. White, E. J. Groth, H. Hasan, K. Noll, P. H. Smith, M. G. Tomasko, and H. A. Weaver 1992. Titan: Evidence for seasonal change—A comparison of Hubble Space Telescope and Voyager images. *Icarus* **96,** 1–9.

Combes, M., and Th. Encrenaz 1984. ESA/NASA Cassini Mission Meeting, London.

Combes, M., L. Vapillon, E. Gendron, A. Coustenis, and Th. Encrenaz 1995a. Spatially resolved imaging of Titan in the near-infrared by adaptive optics. *Proceedings of the 20th General Assembly of the European Geophysical Society,* Hamburg, Germany, 3–7 April. In *Annales Geophysicae,* Vol. 13. Springer Intern.

Combes, M., L. Vapillon, E. Gendron, A. Coustenis, and O. Lai 1995b. Spatially resolved images of Titan in the near-infrared. *Bull. Am. Astron. Soc.* **27,** 52.

Combes, M., L. Vapillon, E. Gendron, A. Coustenis, and O. Lai 1996a. 2-micron images of Titan by means of adaptive optics. *The Messenger* **83,** 40–42.

Combes, M., A. Coustenis, L. Vapillon, E. Gendron, R. Wittemberg, R. Sirdey and O. Lai 1996b. Images of Titan's surface in the near-infrared with ADONIS. *Bull. Am. Astron. Soc.* **28,** 1130.

Combes, M., A. Coustenis, L. Vapillon, E. Gendron, R. Wittemberg, R. Sirdey, and J-P Veran 1997. High resolution imaging of Titan with adaptive optics in the near-infrared. *Proceedings of the 22nd General Assembly of the European Geophysical Society,* Vienna, 21–25 April. In *Annales Geophysicae,* Vol. 15. Springer Intern.

Coustenis, A., B. Bézard, D. Gautier, A. Marten, and R. E. Samuelson 1991. Titan's atmosphere from Voyager infrared observations: III. Vertical distributions of hydrocarbons and nitriles near Titan's north pole. *Icarus* **89,** 152–167.

Coustenis, A., E. Lellouch, J. P. Maillard, and C. P. McKay 1994. Titan's surface: Composition and variability from its near infrared albedo. *Bull. Am. Astron. Soc.* **26,** 1181.

Coustenis, A., and B. Bézard 1995. Titan's Atmosphere from Voyager Infrared Observations: IV. Latitudinal Variations of Temperature and Composition. *Icarus* **115,** 126–140.

Coustenis, A., E. Lellouch, J. P. Maillard, and C. P. McKay 1995. Titan's surface: Composition and variability from its near-infrared albedo. *Icarus* **118,** 87–104.

Coustenis, A., E. Lellouch, B. Schmitt, C. P. McKay, J. P. Maillard, and R. Wittemberg 1996. Surfaces of Titan and other saturnian satellites. *Bull. Am. Astron. Soc.* **28,** 1130.

Coustenis, A., E. Lellouch, M. Combes, R. Wittemberg, C. P. McKay, and J.P. Maillard 1997. Titan's atmosphere and surface from infrared spectroscopy and imaging. In *Astronomical and Biochemical Origins and the Search for Life in the Universe* (C. B. Cosmovici, S. Bowyer, and D. Werthimer, Eds.), pp. 227–234. Proceedings of IAU Colloquium 161.

Flasar, F. M., and B. J. Conrath 1990. Titan's atmosphere: Temperature and dynamics. *Nature* **292,** 693–698.

Gendron, E., P. Léna. 1994. Astronomical adaptive optics: I. Modal control optimization. *Astron. and Astrophys.* **291,** 337.

Gendron, E., and P. Léna 1995. Astronomical adaptive optics: II. Experimental results of an optimized modal control. *Astron. and Astrophys.* **111,** 153.

Griffith, C. A., and T. Owen 1992. Observing the surface of Titan through near-infrared windows in its atmosphere. ESA **SP-338,** pp. 199–204. ESTEC, Noordwijk, The Netherlands.

Griffith, C. A. 1993. Evidence for surface heterogeneity on Titan. *Nature* **364,** 511–514.

Khare, B. N., C. Sagan, E. T. Arakawa, F. Suits, T. A. Callcott, and M. W. Williams 1984. Optical constants of organic tholins produced in a simulated titanian atmosphere: From soft X-ray to microwave frequencies. *Icarus* **60,** 127–137.

Kondo, K., Y. Ichioka, and T. Suzuki 1977. Image restoration by Wiener filtering in the presence of signal-dependent noise. *Appl. Optics* **16**(9), 2554–2558.

Lellouch, E., A. Coustenis, D. Gautier, F. Raulin, N. Dubouloz, and C. Frere 1989. Titan's atmosphere and hypothesized ocean: A reanalysis of the Voyager 1 radio-occultation and IRIS 7.7 $\mu$m data. *Icarus* **79,** 328–349.

Lemmon, M. T., E. Karkoschka, and M. Tomasko 1993. Titan's rotation: Surface feature observed. *Icarus* **103,** 329–332.

Lemmon, M. T., E. Karkoschka, and M. Tomasko 1995. Titan's rotationnal light-curve. *Icarus* **113,** 27–38.

Lunine, J. I., D. J. Stevenson, and Y. L. Yung 1983. Ethane ocean on Titan. *Science* **222,** 1229–1230.

Lunine, J. I. 1993. Does Titan have an ocean? A review of current understanding of Titan's surface. *Rev. Geophys.* **31,** 133–149.

McKay, C. P., J. B. Pollack, and R. Courtin 1989. The thermal structure of Titan's atmosphere. *Icarus* **80,** 23–53.

Muhleman, D. O., A. W. Grossman, B. J. Butler, and M. A. Slade 1990. Radar reflectivity of Titan. *Science* **248,** 975–980.

Muhleman, D. O., A. W. Grossman, and B. J. Butler 1995. Radar investigation of Mars, Mercury and Titan. *Ann. Rev. Earth Planet. Sci.* **23,** 337–374.

Noll, K. S., and R. F. Knacke 1993. Titan: 1–5 $\mu$m photometry and spectrophotometry and a search for variability. *Icarus* **101,** 272–281.

Rigaud, F., G. Rousset, P. Kern, J. C. Fontanella, J. P. Gaffard, F. Merkle, and P. Lena 1991. Adaptive optics on a 3.6 m telescope: results and performances. *Astron. Astrophys.* **250,** 280.

Roddier, F., C. Roddier, and W. Roddier 1988. Curvature sensing: A new wavefront sensing method. *Proc. SPIE* **976,** 203–209.

Sagan, C., and S. F. Dermott 1982. The tide in the seas of Titan. *Nature* **300,** 731–733.

Sagan, C., and S. F. Dermott 1995. Tidal effects of disconnected hydrocarbon seas on Titan. *Nature* **374,** 238–240.

Saint-Pé, O., M. Combes, F. Rigaut, M. Tomasko, and M. Fulchignoni 1993. Demonstration of adaptive optics for resolved imagery of Solar System objects: Preliminary results on Pallas and Titan. *Icarus* **105,** 263–270.

Smith, P. H., and M. T. Lemmon 1993. HST images of Titan. *Bull. Am. Astron. Soc.* **25,** 1105.

Smith, P. H., M. T. Lemmon, R. D. Lorenz, L. A. Sromovsky, J. J. Caldwell, and M. D. Allison 1996. Titan's surface revealed by HST imaging. *Icarus* **119,** 336–349.

Starck, J. L., and F. Murtagh 1993. Richardson–Lucy image restoration with noise suppression based on the wavelet transform. *Proceedings of the 5th ESO/ST-ECF Data Analysis Workshop,* April 1993.

Strong, K., F. W. Taylor, S. B. Calcutt, J. J. Remedios, and J. Ballard 1993. Spectral parameters of self- and hydrogen-broadened methane from 2000 to 9500 $cm^{-1}$ for remote sounding of the atmosphere of Jupiter. *J. Quant. Spectrosc. Radiat. Trans.* **50,** 363–429.

Tomasko, M. G. ESA/NASA Cassini Mission Meeting, London, 1984.

Toon, O. B., C. P. McKay, C. A. Griffith, and R. P.Turco 1992. A physical model of Titan's aerosols. *Icarus* **95,** 24–53.